Article

Fabrication and Characterization of Oxygen-Carbon-Contained CrMnFeCoNi Coatings Electrodeposited in DMF-CH$_3$CN Solution with and without Supporting Electrolyte LiClO$_4$

Tian Xiao [1], Rongguang Wang [2,*] , Eishi Tanabe [3], Yuhki Satoh [4], Mohammed Bazzaoui [5], Yunhan Ling [6] and Zhaoxia Lu [7]

[1] Graduate School of Science and Technology, Hiroshima Institute of Technology, Hiroshima 7315193, Japan
[2] Department of Mechanical Systems Engineering, Hiroshima Institute of Technology, Hiroshima 7315193, Japan
[3] Western Region Industrial Research Center, Hiroshima Prefectural Technology Research Institute, Hiroshima 7390046, Japan
[4] Department of Intelligent Mechanical Engineering, Hiroshima Institute of Technology, Hiroshima 7315193, Japan
[5] Laboratoire des Matériaux et Environnement, Faculté des Sciences, Université Ibn Zohr, Agadir 80060, Morocco
[6] School of Materials Science and Engineering, Tsinghua University, Beijing 100084, China
[7] School of Chemistry and Chemical Engineering, Guangxi University, Nanning 530004, China
* Correspondence: wangrg@cc.it-hiroshima.ac.jp

Abstract: Oxygen-carbon-contained CrMnFeCoNi coatings were electrodeposited in an organic solvent of DMF-CH$_3$CN (N,N-dimethylformamide-acetonitrile) containing chlorides of chromium, manganese, iron, cobalt, and nickel, with or without supporting electrolyte lithium perchlorate (LiClO$_4$). The coatings' composition, structure, hardness, and electrocatalytic properties were examined. The presence of lithium in coatings obtained with LiClO$_4$ showed it unsuitable as a supporting electrolyte in this fabrication process. Without LiClO$_4$, oxygen-carbon-contained CrMnFeCoNi coatings were obtained at constant potentials at −2.0, −2.5, and −3.0 V (vs. SSE) by enhancing the concentrations of the target metal ions in the solution. These coatings were mainly amorphous with nanocrystals, which were comprised of >50 atom% oxygen atoms, >7 atom% carbon atoms, and near equiatomic Cr, Mn, Fe, Co, and Ni, showing a high level of hardness and advanced electrocatalytic activity in the oxygen evolution reaction.

Keywords: oxygen-carbon-contained CrMnFeCoNi coating; lithium perchlorate; organic solvent; electrocatalytic activity; oxygen evolution reaction

1. Introduction

High entropy alloy (HEA) is a solid solutioned metal with a mixing configurational entropy >1.5 R, generally containing five or more constituent elements with individual molar ratios of 5%~35% [1–3]. To date, CrMnFeCoNi [2], ZrNbTaTiW [4], AlCoCrCuFeNi [5], Al$_2$CrFeNiCoCuTi$_x$ [6], AlFeCoCrNi [7], and others have been developed. In particular, Cantor alloy CrMnFeCoNi [2] was first synthesized and studied because of its excellent strength, ductility, toughness, and corrosion resistance [8–11]. Recently, specific catalytic functions were reported in some high entropy oxides (HEOs), such as high catalytic efficiency and stability in oxygen evolution reaction (OER) for (Cr$_{0.2}$Mn$_{0.2}$Ni$_{0.2}$Fe$_{0.2}$Zn$_{0.2}$)Fe$_2$O$_4$ [12]. These excellent properties of HEAs or HEOs generally originate from the high entropy effect in thermodynamics, the lattice distortion effect in structure, the sluggish diffusion effect in dynamics, and the cocktail effect in functions [1]. Thus far, most HEAs and HEOs have been synthesized through casting, sintering, and laser cladding. However, for efficiencies in resource use, weight reduction, corrosion resistance,

hardness, wear resistance, electrocatalytic and electromagnetic properties, coatings of HEAs or HEOs have been synthesized by thermal spraying [13], magnetron sputtering [14–17], and electrodeposition [18–23].

As for electrodeposition of HEAs, Yao et al. produced amorphous coatings of BiFeCoNiMn, NdFeCoNiMn, MgMnFeCoNiGd, and NiFeCoMnBiTm in DMF-CH$_3$CN or DMSO solvent, and the effects of Bi and Fe on magnetic properties of the coatings were investigated [18–21]. Following this, Soare et al. [23] produced amorphous coatings of AlCrFeMnNi and AlCrCuFeMnNi in DMF-CH$_3$CN, and Zheng et al. [22] got an amorphous coating of FeNiCoBiMn in CH$_3$CH-C$_3$H$_7$NO solvent. Using organic DMF-CH$_3$CN, CH$_3$CH-C$_3$H$_7$NO, or DMSO rather than water as the solvent avoids hydrogen evolution. Hydrogen evolution hinders the reduction reaction of target metal ions and consumes much electrical energy. In addition, the supporting electrolyte lithium perchlorate (LiClO$_4$), which improves conductivity in the bath solution, was contained in all organic solvents [18–23].

When a designated potential for reduction is applied in electrodeposition, cations, including lithium-ion (Li$^+$) in the solution, are involved in the electrochemical process. Although the reduction potential of Li$^+$ + e → Li^0 is negative, its accumulation at the electrode might affect deposition by its role in establishing an electric double layer. However, the possibility of deposition of lithium in the electrodeposition of HEAs has not been reported. To enhance conductivity in a bath solution, using concentrated target metal ions instead of supporting electrolyte LiClO$_4$ should be possible. This issue merits investigation.

The solubility of chemicals when adding metal ions into organic solvents is necessary to construct a stable bath solution. Low solubility limits the concentrations of contained target elements in the target coatings. Additionally, elements C, O, and N in a bath solution might be composed into the target coatings during electrodeposition, which could help form high entropy carbides, oxides, or nitrides. The possibility of synthesizing coatings of carbonized, nitridated, or oxidized HEAs in solution merits investigation to clarify the above phenomena.

Furthermore, the applied potential primarily changes the coating composition due to the different reduction potentials of the contained metal ions. In solutions containing multi-metal ions, the reduction behavior of each metal ion might differ from that in the solution containing isolated-metal ions. Therefore, the co-deposition behavior of multi-metal ions is expected. Investigation of the above issues is essential to develop an efficient and robust applicable electrodeposition process for functional coatings.

As a fundamental study to clarify the above issues, here in this work, the target elements of Cr, Mn, Fe, Co, and Ni in the Cantor alloy are selected as the research subject, considering the different solubility of their chlorides as well as their hydrous chemicals. After investigating the individual reduction behavior of each metal ion, the coatings containing Cr, Mn, Fe, Co, and Ni were electrodeposited under designated potentials in DMF-CH$_3$CN solvent containing chlorides of chromium, manganese, iron, cobalt, and nickel. The supporting electrolyte of LiClO$_4$ was included or excluded from the solution to investigate the affection of Li$^+$. Finally, the mechanical and electrocatalytic properties of the coatings were investigated.

2. Experimental

Copper (Cu) plates (99.98% pure, 20 mm × 15 mm × 1 mm) as the substrate for electrodeposition were polished with #2000 waterproof emery paper and ultrasonically rinsed in deionized water and acetone before connecting an electrical feed wire to the backside.

Electrodeposition was performed in a glass breaker containing organic solvent-based bath solutions at 313 ± 1 K. An electrochemical workstation (CS350, Wuhan Corrtest Inst. Co., Wuhan, China) was used to apply a constant potential: a saturated silver/silver chloride electrode (SSE, 0.1976 V vs. reversible hydrogen electrode (RHE)) was used as the reference electrode and a platinum plate as the counter electrode. In the bath solution, designated metal chlorides: CrCl$_3$·6H$_2$O, MnCl$_2$, FeCl$_2$·4H$_2$O, CoCl$_2$, and NiCl$_2$·6H$_2$O, were added to the DMF-CH$_3$CN (4:1 by volume) solvent. Unlike other reports [18–21],

we confirmed the insolubility of anhydrous chlorides $CrCl_3$ and $NiCl_2$ in the solvent. Therefore, chemicals $CrCl_3 \cdot 6H_2O$ and $NiCl_2 \cdot 6H_2O$ were used. $FeCl_2 \cdot 4H_2O$ was chosen due to availability.

As shown in Table 1, solutions A and B were prepared for the deposition. Further, 0.1 M $LiClO_4$ as the supporting electrolyte was contained in only solution A. The composition of solution B was adjusted to obtain equal molar ratios of Cr, Mn, Fe, Co, and Ni in coatings. After dissolving the metal chlorides or $LiClO_4$ in the solvent, the solutions were dehydrated with molecular sieves (4A 1/8, Fujifilm Wako Pure Chemical Co., Osaka, Japan) for 43.2 ks, then deaerated by nitrogen gas (purity: 99.999%) for 3.6 ks before and during the deposition, with the molecular sieves remaining at the bottom of the solution.

Table 1. Solutions for electrodeposition: metal chlorides with various concentrations in an organic solvent of DMF and CH_3CN (4:1 by volume).

Electrolyte	$CrCl_3$ (M)	$MnCl_2$ (M)	$FeCl_2$ (M)	$CoCl_2$ (M)	$NiCl_2$ (M)	$LiClO_4$ (M)	Total Cations (M)
A	0.01	0.01	0.01	0.01	0.01	0.10	0.15
B	0.06	0.10	0.04	0.06	0.02	-	0.28

Potentials for triggering the reduction reaction of the respective metal ions on a Cu substrate with a diameter of 1.0 mm were investigated in an organic solvent containing chlorides of different metals by measuring the cyclic voltammetry (CV) curves at the scanning rate of 100 mV/s. Before CV measurement or electrodeposition, note that substrates were rinsed in 5% hydrochloric acid, distilled water, and acetone. Based on these measurements, the deposition in solutions A and B on the Cu plate was performed at −2.0 V, −2.5 V, and −3.0 V (vs. SSE) for 0.6 and 1.8 ks.

Images of the surface and cross-section profiles of electrodeposited coatings were obtained by a scanning electron microscope (SEM; JOEL-6510A, JEOL Ltd., Tokyo, Japan), and their crystal structures by grazing-incidence X-ray diffraction (DMAX-2500, Rigaku Co., Tokyo, Japan) with Cu Kα excited at 40 kV and 150 mA, X-ray incidence angle 1.0°, scanning step of 0.02°, step analysis time of 0.6 s. Furthermore, a cross-sectional slice thinner than 100 nm obtained by 40 kV accelerated Ga^+ in a focus ion beam (FIB) (FB2100, Hitachi High-Technologies Co., Tokyo, Japan) after sequential deposition of carbon and tungsten, was investigated by a 297 kV accelerated electron beam with a focused diameter of 1 nm in a field emission scanning electron microscope (FE-STEM; JEM-3000F, JEOL Ltd., Tokyo, Japan).

The composition was analyzed using an energy dispersive X-ray spectrometer (SEM-EDS; JED-2300, JEOL Ltd.). X-ray photoelectron spectroscopy (XPS; AXIS ULTRA, Shimadzu Co., Kyoto, Japan) was used to analyze chemical binding among coating elements (analysis area: 2 mm × 1 mm) in a vacuum chamber under air pressure $<4 \times 10^{-5}$ Pa. The X-ray was Mg Kα excited 15 kV and 10 mA. The pass energy was set as 40 eV. Before XPS analysis, the specimen surface was sputter-etched for 6.0 ks by accelerated argon ions (Ar^+) to eliminate contaminants and surficial oxide. A mixed Gauss–Lorentz function as 0.7:0.3 was used to split element peaks according to the binding energy of each chemical state. In addition, Time-of-Flight Secondary Ion Mass Spectrometry (TOF-SIMS; Thermo Fisher Scientific, Waltham, MA, USA) analysis was conducted in a selected surface fracture to determine the presence of lithium in the coating.

Coating hardness was measured by nanoindentation (DUH-201, Shimadzu Co.) to a maximum load of 40 nN. OER electrocatalytic property was evaluated in an aerated 1.0 M KOH aqueous solution (pH = 13.8) at 303 ± 1 K by measuring linear sweep voltammetry (LSV) at a scanning rate of 5 mV/s. The potential was converted versus RHE, $E_{RHE} = E_{Ag/AgCl} + 0.060 \times pH + 0.1976$ (V), and the Tafel slope was obtained from the LSV curve in the kinetically controlled region.

3. Results and Discussion

3.1. Cyclic Voltammetry and Chronoamperometry Curves

Figure 1a shows the CV curves obtained on the Cu disk (1.0 mm dia.) in DMF-CH$_3$CN with and without LiClO$_4$. In the absence of LiClO$_4$ (black line), reaction peaks are not observed, regardless of dehydration by molecular sieves or not, demonstrating high stability of DMF-CH$_3$CN solvent in the potential scope of −3.0~0.0 V (vs. SSE). In the presence of 0.1 M LiClO$_4$ in solution without dehydration (red line), a small peak at −0.69 V and two wide peaks were observed near −1.92 V and −2.76 V (vs. SSE). After dehydration (blue line), the peak at −1.92 V degenerated to two smaller ones at −1.66 V and −2.11 V, while those at −0.69 V and −2.76 V became much weaker.
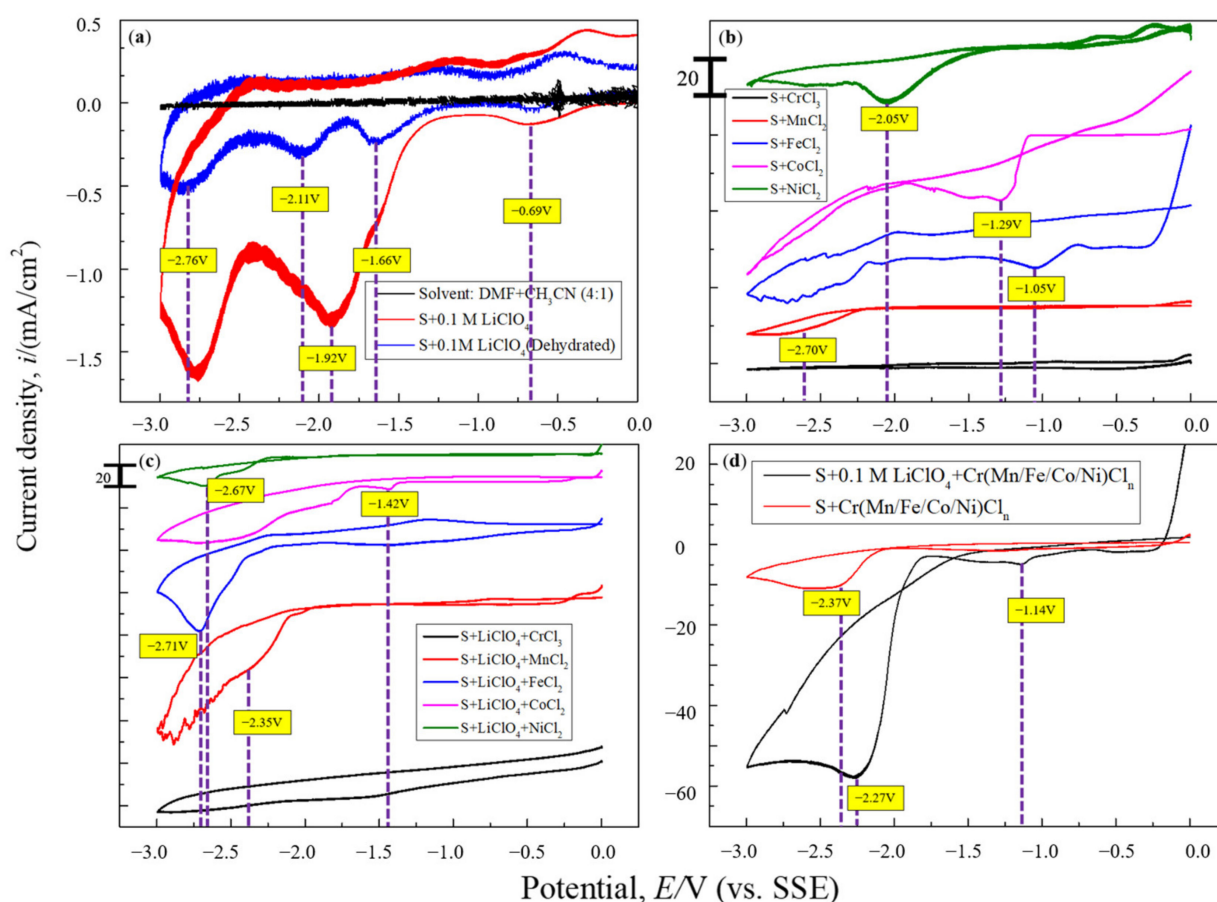

Figure 1. Cyclic voltammetry curves obtained on a Cu disk (Φ: 1 mm) in DMF-CH$_3$CN (4:1 by volume) solution at a sweep rate of 100 mV/s. (**a**) Without and with 0.1 M LiClO$_4$; (**b**) Containing isolated 0.01 M FeCl$_2$, CoCl$_2$ or 0.02 M CrCl$_3$, MnCl$_2$, NiCl$_2$ without LiClO$_4$; (**c**) Containing isolated 0.01 M FeCl$_2$, CoCl$_2$ or 0.02 M CrCl$_3$, MnCl$_2$, NiCl$_2$ with 0.1 M LiClO$_4$; (**d**) Containing 0.01 M CrCl$_3$, 0.01 M MnCl$_2$, 0.01 M FeCl$_2$, 0.01 M CoCl$_2$, and 0.01 M NiCl$_2$ with and without 0.1 M LiClO$_4$.

In preliminary XPS analysis, lithium was not detected from the copper surface after hydration and applying a potential of −2.5 V in the 0.1 M LiClO$_4$-containing DMF-CH$_3$CN solution without the target metal ions. In contrast, a peak of Li 1s was observed under the potential of −3.0 V. Therefore, the peak at −2.76 V was considered to correspond to the reduction reaction of Li$^+$ + e → Li^0, which is much nobler than that equilibrium value of −3.24 V vs. SSE (0.1 M LiClO$_4$ solution at 313 K). A more negative reduction potential of Li$^+$ was reported in an aqueous solution due to high hydration enthalpy [24]. Therefore, the weak hydration of Li$^+$ in the current organic solution might have promoted the above reduction. The peaks at −0.69 V and −2.11 V might correspond to the two-step oxygen reduction of O$_2$ → O$_2^-$ and O$_2^-$ → O$_2^{2-}$ [25], whereas the peak at −1.66 V might

correspond to the reduction of dissolved water [26]. Water comes from $LiClO_4$ without dehydration, while oxygen originates from adsorbed air in the porous molecular sieves.

Figure 1b shows the CV curves in solutions containing isolated chloride: $FeCl_2$, $CoCl_2$ at 0.01 M or $CrCl_3$, $MnCl_2$, $NiCl_2$ at 0.02 M. $LiClO_4$ was absent from all solutions. Dehydration and deaeration were applied before measurement. No reaction peak was detected in the $CrCl_3$ solution, indicating the difficulty of the reduction of Cr^{3+}. In contrast, reaction peaks were observed at −2.70 V for $MnCl_2$, −1.05 V for $FeCl_2$, −1.29 V for $CoCl_2$, and −2.05 V for $NiCl_2$, respectively. The current peaks in Figure 1b are larger than those in Figure 1a. According to the XPS analysis of isolated coatings obtained at −3.0 V from the above solutions (Supplementary Materials Figure S1), chromium and manganese showed a fully oxidized state (Cr^{3+}, Mn^{2+}), whereas iron, cobalt, and nickel, respectively, appeared at their elemental and oxidized states. Therefore, the current peaks in $FeCl_2$, $CoCl_2$, or $NiCl_2$ solution surely correspond to the reduction of the metal ions. The reduction of Cr^{3+} in the $CrCl_3$ solution is not evident from the CV curve and the XPS spectrum. Hence, the Cr^{3+} state in the obtained coating is ascribed to a direct chemical deposition. On the other hand, the current peak that appeared in the $MnCl_2$ solution is considered as the reduction of Mn^{2+} but without direct XPS evidence. The oxidized state of metals can be obtained during or after the deposition. Further clarifying the mechanism of the direct oxidization during the deposition should help enhance the quality of the coating.

Figure 1c shows the CV curves in 0.1 M $LiClO_4$-containing solutions with isolated chloride: $FeCl_2$, $CoCl_2$ at 0.01 M or $CrCl_3$, $MnCl_2$, $NiCl_2$ at 0.02 M, after dehydration and deaeration. As in Figure 1b, reaction peaks are not seen in the $CrCl_3$ solution, while the current density in the $MnCl_2$ solution became larger after −2.5 V. The reaction peaks were obtained at −2.35 V for $MnCl_2$, −2.71 V for $FeCl_2$, −1.42 V for $CoCl_2$, and −2.67 V for $NiCl_2$. The potentials for $FeCl_2$ and $NiCl_2$ became negative compared to those in Figure 1b. These potentials differ from those reported by Yao et al. [18–21] and Soare et al. [23], perhaps due to the use of hydrous chemicals. The reason is unclear, but $LiClO_4$ surely affected the reduction potential of each target metal ion, especially, the current density after −2.5 V became large.

Figure 1d shows the CV curves obtained in the solution of 0.01 M $CrCl_3$ + 0.01 M $MnCl_2$ + 0.01 M $FeCl_2$ + 0.01 M $CoCl_2$ + 0.01 M $NiCl_2$ with and without 0.1 M $LiClO_4$. Dehydration and deaeration were applied before measurement. The reduction current at −1.14 V was relatively larger with than without $LiClO_4$. In addition, the large currents between −2.0 V and −3.0 V might be related to co-deposition of multi-metal ions. The reduction of Li^+ might also be involved in the case of solutions containing $LiClO_4$.

Based on these CV measurements, potentials −2.0 V, −2.5 V, and −3.0 V (vs. SSE) were chosen to conduct electrodeposition. Figure 2a shows the chronoamperometry curves in solution A: 0.01 M $CrCl_3$ + 0.01 M $MnCl_2$ + 0.01 M $FeCl_2$ + 0.01 M $CoCl_2$ + 0.01 M $NiCl_2$ with 0.1 M $LiClO_4$. The higher the applied negative-potential, the higher the resultant negative-current. The current continuously and largely decreased with deposition time, indicating instability of the electric double layer with the involvement of Li^+. The sharply decreased current might correspond to the largely decreased sum of Li^+ ions near the electrode due to reduction. A more extended period was needed to reach a stable state at −3.0 V, indicating a continuous accumulation of lithium ions at the electric double layer. Figure 2b shows the chronoamperometry curves in solution B: 0.06 M $CrCl_3$ + 0.1 M $MnCl_2$ + 0.04 M $FeCl_2$ + 0.06 M $CoCl_2$ + 0.02 M $NiCl_2$ in $DMF-CH_3CN$ without $LiClO_4$. The current sharply decreased after applying a designated potential and reached a stable value: higher negative-current under higher negative-potential. The rapid decrease of current in the initial 50 s should be related to the rapid formation of a stable electric double layer containing various metal ions. Some metal ions migrated to the Cu surface, and deposition occurred.
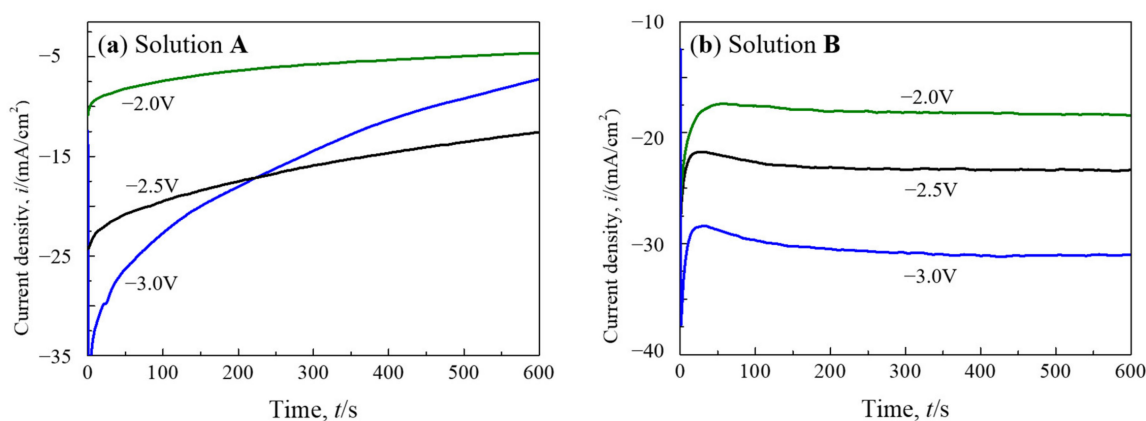
Figure 2. Potentiostatic chronoamperometry curves on a Cu plate at applied potentials of −2.0 V, −2.5 V, and −3.0 V (vs. SSE) in solutions A (**a**) and B (**b**).

3.2. Surface and Cross-Section

Coatings A and B were obtained from solutions A and B, respectively. When deposition-finished coating A was removed from the solution and immediately put into water for rinse, gas bubbled from the surface accompanying dissolution of the coating. More bubbles appeared on specimens obtained at higher negative-potentials. Therefore, the solvent of DMF and CH_3CN followed by acetone, was selected instead of water to rinse coating A. The coating surface changed from black to white with 1-day storage in a desiccator containing dry air. The higher the negative-potential applied, the wider the white area appeared. In contrast, coating B was stable in either water or air.

Figure 3 shows the surface features of coatings A and B deposited at −2.0 V, −2.5 V, and −3.0 V (vs. SSE) for 0.6 ks. In coating A (Figure 3(a_1–a_3)), rod- and lump-like particles were evident, along with some cracks. The fracture surface of the crack was examined in the composition analysis in Section 3.4. On coating B (Figure 3(b_1–b_3)), uniform spherical particles were observed, and no cracks were present.

Figure 4 shows the cross-section of coating B deposited at −2.0 V and −3.0 V. Depending on the potential applied and deposition duration, the thickness ranges from 0.5 to 2.0 μm. Higher negative-potential promoted coating thickness. No delamination or vertical cracks are evident, resulting in good compactness and integrity. A comparative cross-section view of coating A was unavailable due to equipment constraints (wire cut electrical discharge machine). In contrast, in coating A (−2.5 V; 0.6 ks), a FIB-machined cross-sectional slice by the following TEM analysis revealed two layers, an outer one (thickness: 0.8 μm) and an inner one (thickness: 2.7 μm) without delamination.

3.3. Crystal Structure

Figure 5 compares pre- and post-coated grazing-incidence X-ray diffraction patterns. The diffraction peaks of Cu (111), (200), and (220) were detected in the copper plate. Among coating A, diffraction peaks of Li_2CO_3 (002), (402), and (424) or the peak of Li_2O (220) were confirmed. Contaminated NaCl (200) might be overlayed with Li_2CO_3 (200). Note that sodium is contained in the molecular sieves. Higher negative-potential, higher diffraction peaks appeared. Under the same applied potential, −2.5 V or −3.0 V, for a more extended deposition period, the diffraction intensity of Li_2CO_3 (200) became weaker. Conversely, these diffraction peaks at −2.0 V became more apparent with a longer deposition time. Diffraction patterns among coating B greatly differed from those among coating A. The longer the deposition time, the weaker the diffraction intensity, with peaks of Cu (200) and (220) almost absent from the 1.8 ks deposited specimen. No other peaks were detected. Therefore, coating B was confirmed as either amorphous or nanocrystalline. These XRD results correspond with previous reports [18–23], where post-heat treatment can obtain apparent crystallization.
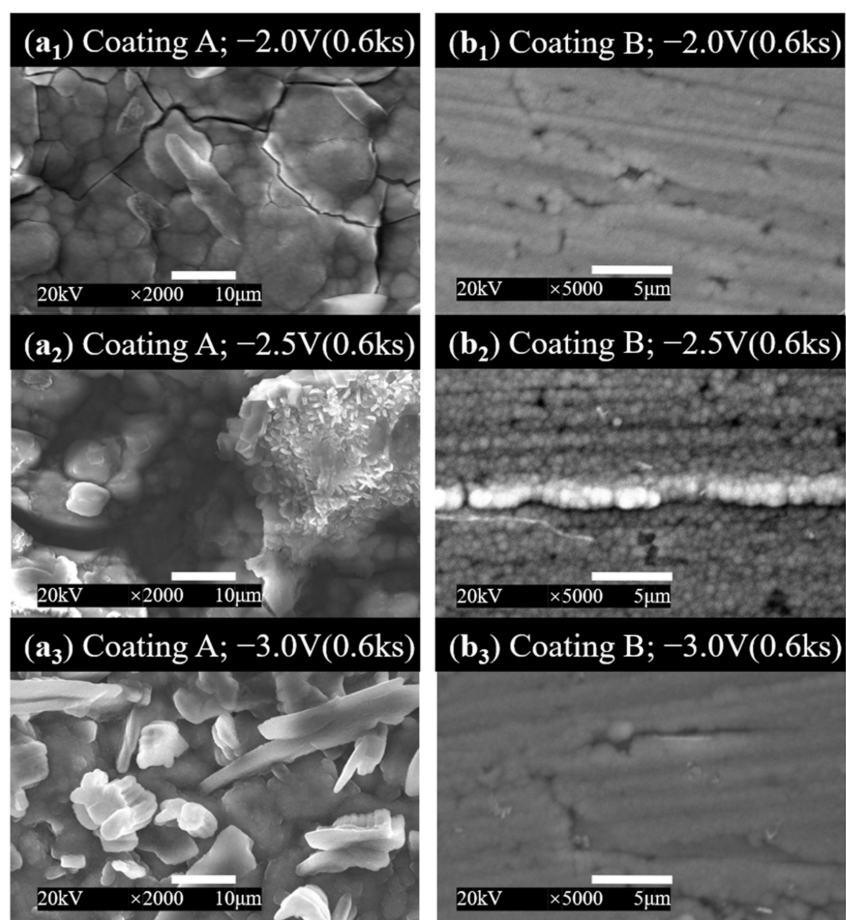
Figure 3. Surface morphologies of coatings A (**a₁**–**a₃**) and B (**b₁**–**b₃**) deposited at −2.0 V, −2.5 V, and −3.0 V (vs. SSE) for 0.6 ks.
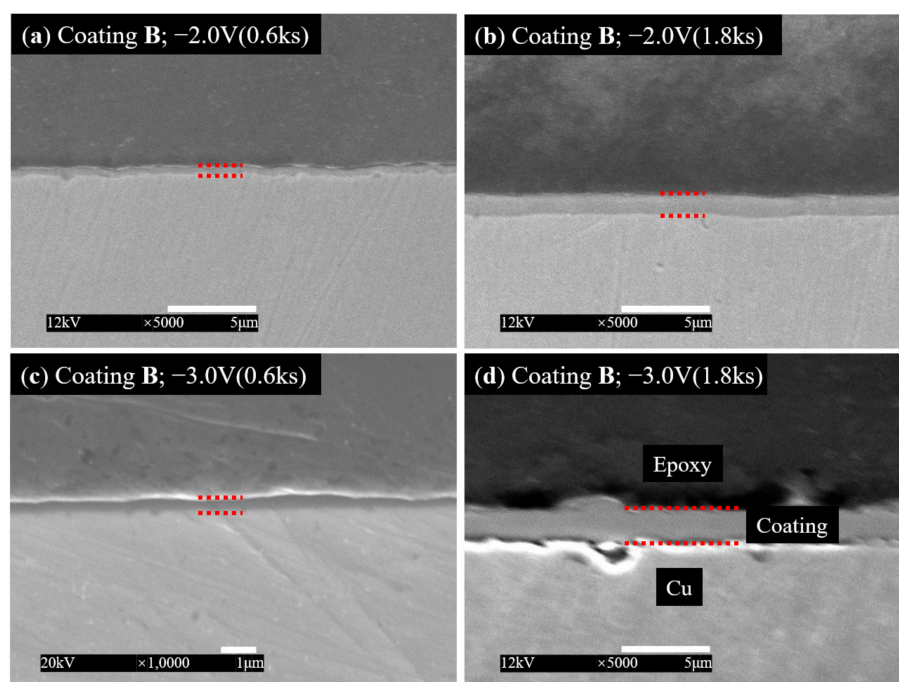

Figure 4. Cross-section of coating B deposited at −2.0 V (**a,b**) and −3.0 V (vs. SSE) (**c,d**) for 0.6 ks and 1.8 ks.
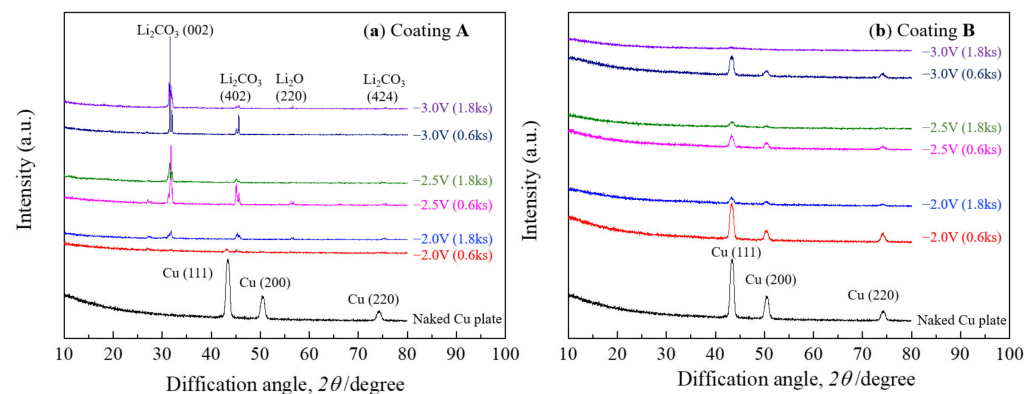
Figure 5. Grazing-incidence X-ray diffraction patterns of coatings A (**a**) and B (**b**) deposited at −2.0 V, −2.5 V, and −3.0 V (vs. SSE) for 0.6 ks and 1.8 ks, with an incidence angle of 1.0°.

Figure 6 shows the results of TEM analysis of cross-sectional slices of coatings A (−2.5 V, 0.6 ks) and B (−2.5 V, 0.6 ks). The bright-field images (a_1,b_1) confirmed that coating A was thicker than coating B. As described before, two layers were observed in coating A. From the bright-field image (a_2,b_2), more nanocrystals were observed in the inner layer of coating A than B. The selected area electron diffraction (SAED) pattern (a_3,b_3) also confirmed a fine structure containing the main amorphous and some nanocrystals for coating B or the inner layer of coating A. According to Figure 6(a_4,a_5), the outer layer is almost wholly composed of nanocrystals. These results agree with the XRD data in Figure 5.
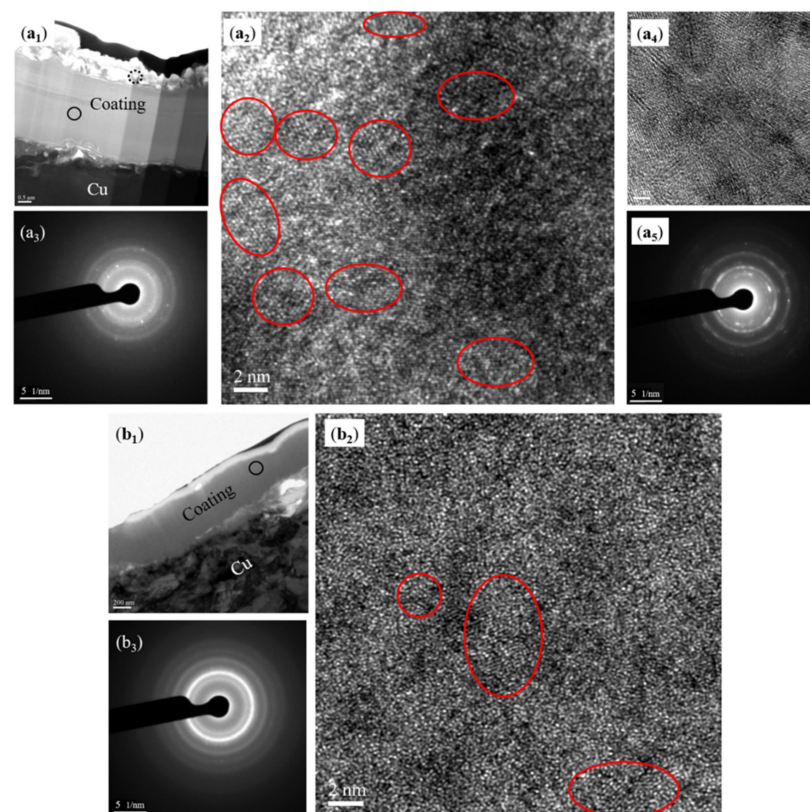

Figure 6. Bright-field images at low- (a_1,b_1) and high-magnification (a_2,a_4,b_2), and selected area electron diffraction (SAED) patterns (a_3,a_5,b_3) from the solid circles (a_1,b_1) and dot circle (a_1). (a_1–a_5): Coating A obtained at −2.5 V (vs. SSE) for 0.6 ks; (b_1–b_3): Coating B obtained at −2.5 V (vs. SSE) for 0.6 ks; (a_2): observed from the inner layer (a_1); (a_4): observed from the out layer (a_1); (a_3): SAED from the solid circle in (a_1); (a_5): SAED from the dot circle in (a_1); (b_3): SAED from the solid circle in (b_1).

3.4. Composition and Chemical State

The composition of coatings was analyzed by SEM-EDS. Figure 7 shows the molar fractions of Cr, Mn, Fe, Co, Ni, O, and C in coatings A and B, which were obtained at −2.0 V, −2.5 V, and −3.0 V (vs. SSE) for 0.6 ks. Both coatings' five targeted metal elements (Cr, Mn, Fe, Co, and Ni) were approximately equal regardless of applied potential. In both coating A and B, more than 50 at. % oxygen and more than 7 at. % carbon were detected. Table 2 shows coating B's compositions and mixed configuration entropies after electrodeposition for 0.6 ks. Here, ΔSm_7 and ΔSm_5 are the mixing entropies calculated from all elements (C, O, Cr, Mn, Fe, Co, Ni) and from only five metals (Cr, Mn, Fe, Co, Ni), respectively. High entropies were confirmed from each coating.
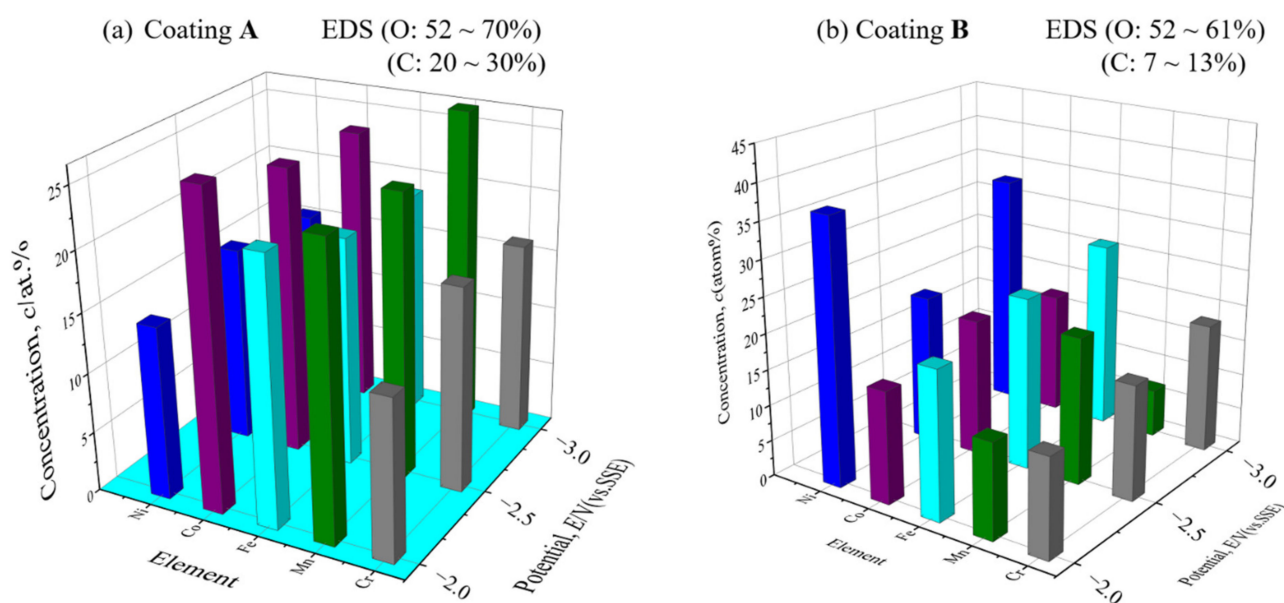

Figure 7. Atomic percentage of oxygen (O) and carbon (C) elements in coatings A (**a**) and B (**b**) deposited at −2.0 V, −2.5 V, and −3.0 V (vs. SSE) for 0.6 ks. Compositions were obtained by energy dispersive X-ray spectrometer (EDS).

Table 2. Compositions and mixed configuration entropies ($\Delta Sm7$, $\Delta Sm5$) of coatings obtained in solution B for 0.6 ks.

Applied Potential (V vs. SSE)	Atomic Percentage of Element (at. %)							ΔSm_7 *	ΔSm_5 **
	Cr	**Mn**	**Fe**	**Co**	**Ni**	**O**	**C**	**(J·K^{-1}·mol^{-1})**	**(J·K^{-1}·mol^{-1})**
−2.0	4.74	4.58	7.14	5.41	12.8	52.57	12.76	1.50 R ***	1.52 R
−2.5	5.04	6.43	7.54	6.00	6.47	60.96	7.56	1.37 R	1.60 R
−3.0	5.66	2.09	8.16	5.32	10.23	55.61	12.93	1.43 R	1.50 R

* ΔSm_7: containing elements O, C, Cr, Mn, Fe, Co, and Ni; ** ΔSm_5: containing elements Cr, Mn, Fe, Co, and Ni; *** R = 8.314 J/(mol·K).

Figures 8 and 9 show XPS spectra of coatings A and B after Ar$^+$ sputter etching for 6.0 ks. The etched depth of about 20 nm (vs. SiO$_2$) was sufficient to remove contaminants and surficial oxides.
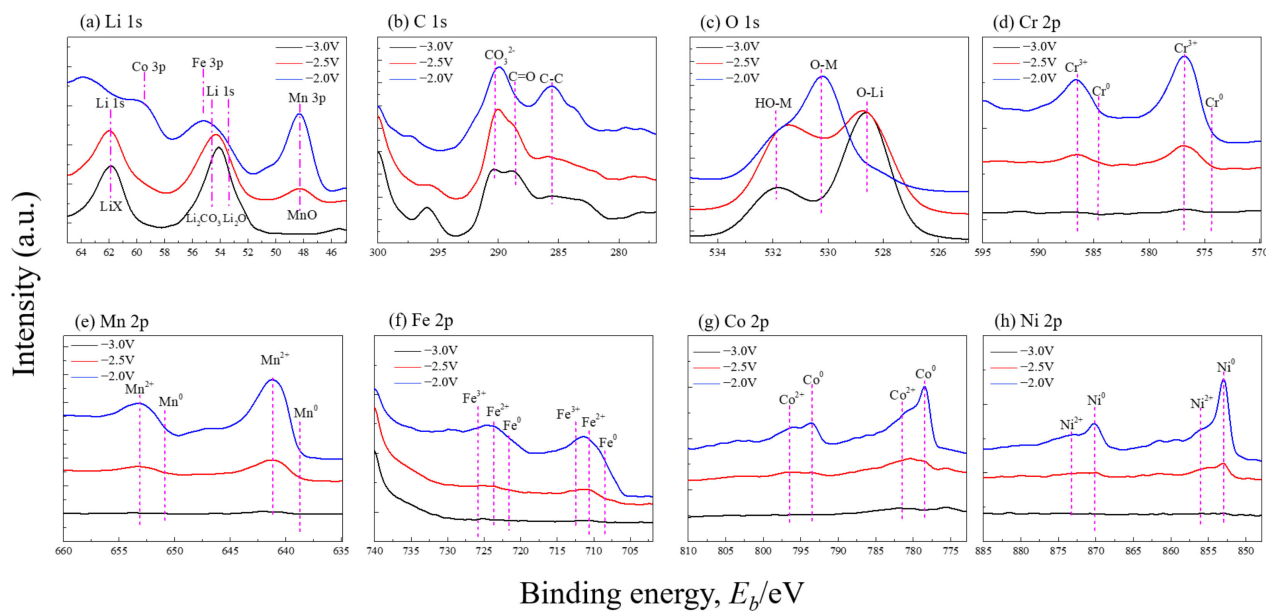
Figure 8. XPS spectra of Li 1s (**a**), C 1s (**b**), O 1s (**c**), Cr 2p (**d**), Mn 2p (**e**), Fe 2p (**f**), Co 2p (**g**), and Ni 2p (**h**) from coating A obtained at −2.0 V, −2.5 V, and −3.0 V (vs. SSE) for 0.6 ks.
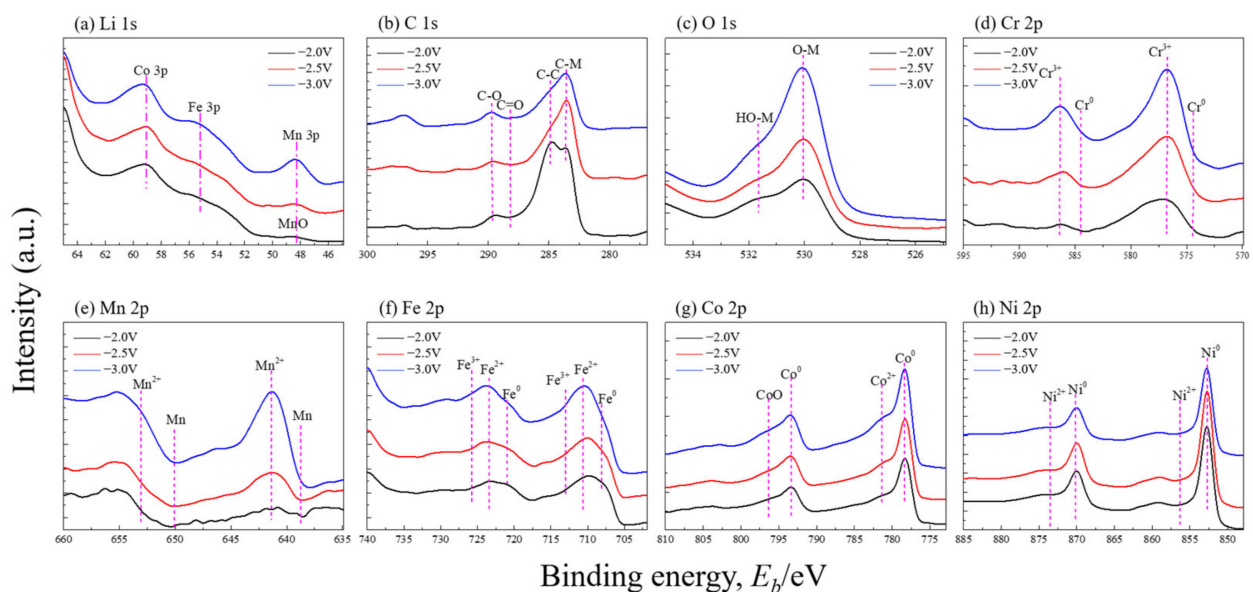
Figure 9. XPS spectra of Li 1s (**a**), C 1s (**b**), O 1s (**c**), Cr 2p (**d**), Mn 2p (**e**), Fe 2p (**f**), Co 2p (**g**), and Ni 2p (**h**) from coating B obtained at −2.0 V, −2.5 V, and −3.0 V (vs. SSE) for 0.6 ks.

Peak deconvolution was conducted for each chemical state. Only the central positions are shown for visual effect. From TEM observation (Figure 6(a_1)), we know all the spectra for coating A were obtained from the outer layer. In coating A (−3.0 V, black lines), 2p peaks of Cr, Mn, Fe, Co, and Ni did not appear. In contrast, high O 1s and Li 1s were clearly detected. Further, from a preliminary TEM-EDS mapping of the cross-section, fewer elements Cr, Mn, Fe, Co, and Ni were detected in the outer- than inner-layer. Therefore, lithium may have been included in the coating during electrodeposition and formed the lithium-enriched outer layer afterward. This may explain the dissolution in water with bubbles. As described in Section 3.1, Li^+ can be reduced to Li^0 in the isolated $LiClO_4$-containing solution at −3.0 V. Therefore, from analysis of C 1s, O 1s, and Li 1s, the formation of Li_2CO_3 and Li_2O can be confirmed in the outer layer. Li_2CO_3 and Li_2O correspond to binding energies 54.6 eV and 53.5 eV, respectively. Lithium generally combines O_2 and CO_2

in the air to form Li_2CO_3 [27], which corresponds to the white appearance of the outer layer after air exposure. Large amounts of lithium in this coating and subsequent formation of Li_2CO_3 and Li_2O may have led to local stress resulting in the cracks observed (Figure 3(a_1)). With increasing the applied potential to -2.5 V or -2.0 V, the intensity of Li 1s decreased, and the 2p spectra of Cr, Mn, Fe, Co, and Ni appeared. The inclusion of lithium in coatings at -2.5 V, perhaps, is attributed to a reduction of Li^+ promoted by other metal ions. At -2.0 V, the five 2p spectra of the target elements reached their highest values. Cr^{3+} and Mn^{2+} were observed at 576.6 eV and 641.3 eV, but without the appearance of Cr^0 and Mn^0. Meanwhile, Fe 2p was deconvoluted into Fe^{3+}, Fe^{2+}, and Fe^0; Co^{2+}, Co^0, Ni^{2+}, and Ni^0 were respectively distinguished from Co 2p and Ni 2p. In addition, the O 1s spectrum can be deconvoluted into O(-Li), O(-M), and HO(-M). The corresponding binding energies [28] are listed in Table 3.

Table 3. Binding energies of Li 1 s, C 1 s, O 1 s, Cr 2p, Mn 2p, Fe 2p, Co 2p, and Ni 2p spectrum.

Photo Peak	Li 1s		Cr 2p3/2	Mn 2p3/2	Fe 2p3/2			Co 2p3/2		Ni 2p3/2	
Component	Li_2O	Li_2CO_3	Cr^{3+}	Mn^{2+}	Fe^0	Fe^{2+}	Fe^{3+}	Co^0	Co^{2+}	Ni^0	Ni^{2+}
Binding energy (eV)	53.5	54.6	576.6	641.3	708.4	710.7	713.7	778.4	781.2	852.9	856.3

Photo peak	C 1s				O 1s				
Component	C-C	C=O	CO_3^{2-}	C-M	C-O	O-Li	O(-M)	O(-OH)	
Binding energy (eV)	285.7	287.8	290.0	283.4	289.8	528.6	530.2	531.8	

On either coatings B (Figure 9), the 2p spectra of Cr, Fe, Co, and Ni appeared. Mn peak was not detected at -2.0 V but was at -2.5 V and -3.0 V. Either of the above elements showed similar chemical states as coating A (-2.0 V vs. SSE). The peaks of C-C, C-M, HO-M, and O-M were confirmed from C 1s and O 1s. With higher negative-potentials, the C-M peak went over C-C, and the ratio of O-M to HO-M became larger. In Figure 9a, except for the 3p spectra of Fe, Co, and Mn, the Li 1s peak did not appear due to the absence of $LiClO_4$ in the solution.

Figure 10 shows atomic concentrations of elements at their detailed chemical states according to deconvoluted peaks. The symbol "M" means the five target metals without lithium. In coating A (Figure 10a), the amounts of C-C (organic contaminant), CO_3^{2-}, and C=O were calculated, showing the appearance of C=O under higher negative-potential. For oxygen, compared to O(-M) and HO(-M), O(-Li) is the primary state. By decreasing the potential to -3.0 V, the Li content increased to near 55 at. %, while the total content of Cr, Mn, Fe, Co, and Ni sharply decreased to near zero. In coating B (Figure 10b), except for Ni at -3.0 V, the contents of Cr, Mn, Fe, and Co gradually increased as the applied potential decreased. Only a little Ni^{2+} was detected as compared to Ni^0. Fe^{2+} and Fe^{3+} occupied about 87% of total iron (9–11 at. %), while Co^{2+} was about half of the total cobalt (11 at. %). For Cr and Mn, except Cr^{3+} and Mn^{2+}, no elemental Cr^0 and Mn^0 were detected. With the decrease of the potential, oxygen increased while carbon decreased. The total oxygen content was at 22–39 at. %, in which O(-M) was the main component. The XPS-analyzed oxygen concentration is about half of that EDS-analyzed one. Note that oxygen in the outer layer of coatings A existed mainly as Li_2CO_3 and Li_2O, while in coatings B, it mainly formed oxides and hydroxides of the target metals.
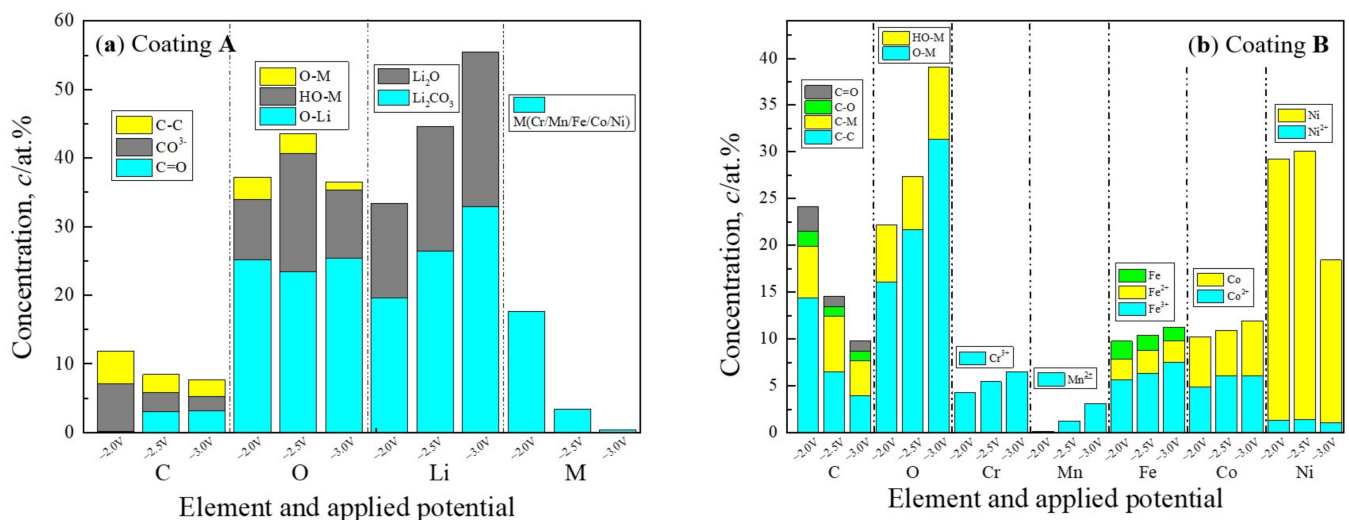
Figure 10. Quantitative concentration of elements obtained in coating A (**a**) and coating B (**b**) from Figures 8 and 9 (XPS analysis).

Figure 11 shows the mapping for lithium on a fracture surface of coating A (-2.5 V vs. SSE; 0.6 ks). Lithium was detected from the coating surface to the copper substrate, demonstrating that lithium was trapped within the coating.
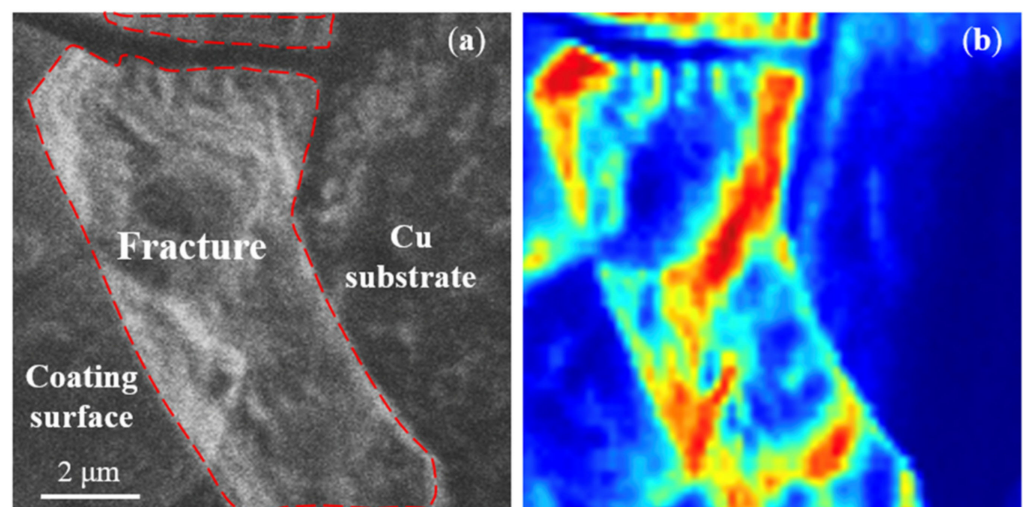

Figure 11. A fracture surface of coating A (-2.5 V vs. SSE; 0.6 ks) (**a**) and its lithium mapping by TOF-SIMS (**b**). Lithium was detected from the red and the light zones in (**b**).

3.5. Reactions in Electrodeposition

In solution A, Li^+ participates in constructing the electric double layer under a designated potential. With the initial deposition of M (Cr, Mn, Fe, Co, or Ni), more and more Li^+ concentrates in the electric double layer, reducing target element deposition. When the lithium ions reach a threshold concentration, the reduction of Li^+ to Li^0 occurs. The inclusion of lithium in the coating might also be related to the effect of co-deposition with other metal ions.

In solution B, without Li^+ to participate the electric double layer, the deposition current quickly became stable. The origin of contained oxygen and carbon in the coating is a big issue. Carbon should be originated from organic solvents. In a preliminary experiment using only anhydrous chemicals $MnCl_2$, $FeCl_2$, and $CoCl_2$, a MnFeCo coating with near 50 at. % containing oxygen was confirmed. Therefore, it is reasonable to consider that the contained oxygen atoms came mainly from DMF (C_3H_7NO). However, the details are unclear and worth further investigation. On the other hand, the bound water in $CrCl_3 \cdot 6H_2O$, $FeCl_2 \cdot 4H_2O$, and $NiCl_2 \cdot 6H_2O$ should also provide some oxygen to the coating according to the CV curves (Figure 1a). It is known that $CrCl_3 \cdot 6H_2O$ firstly ionized to a compact octahedron structured $[Cr(H_2O)_6]^{3+}$ in the current solution [29]. Similar hydration or solvation phenomena might also occur for Mn^{2+}, Fe^{2+}, Co^{2+}, and Ni^{2+}. Such complexes should have varied the reduction potential of metal ions and therefore affected the co-deposition behavior.

Similar to what occurred in the isolated $CrCl_3$ solution, the whole formation of oxide/hydroxide of chromium here indicates that reduction of Cr^{3+} did not occur. The reduction of Mn^{2+} is still not evident from the XPS analysis in Figures 8 and 9. On the other hand, the reduction of iron, cobalt, and nickel ions occurred, with partial or complete oxidation happening during or after the deposition.

According to the above analysis, the synthesized coatings are not the pure metal of CrMnFeCoNi but oxygen-carbon-contained ones, which contain some carbon atoms near that so-called HEO. The ratio of the high-valent metal of M^{m+}/M in coating B decreased from Cr^{3+}/Cr, Mn^{2+}/Mn, Fe^{n+}/Fe, Co^{2+}/Co, to Ni^{2+}/Ni, seemingly related to a decrease in unpaired electrons in the 3d and 4s orbitals in the order of Cr, Mn, Fe, Co, and Ni. Oxygen atoms bound to all atoms of Cr and Mn, most atoms of Fe, half of Co, and a few Ni atoms, perhaps leaving a certain amount of oxygen or carbon vacancies. Analyses of X-ray diffraction and TEM suggest this coating was almost amorphous without oxides and carbides with a uniform distribution of its elements. Furthermore, the supporting electrolyte of $LiClO_4$ was proven detrimental to the above electrodeposition. Knowledge obtained from this study can be applied to the deposition of other elements to pursue novel functions or properties.

3.6. Mechanical and Electrocatalytic Properties

Plastic hardness values of coating B (deposition time: 1.8 ks) obtained under maximum load 40 nN were 2670 MPa (−2.0 V vs. SSE), 2660 MPa (−2.5 V), and 2250 MPa (−3.0 V), which exceed the copper substrate hardness of 1600 MPa.

Figure 12 shows the polarization LSV curves (a) and the Tafel slopes (b) of Cu, RuO_2, and coatings deposited at −2.0 V, −2.5 V, and −3.0 V (vs. SSE) for 0.6 ks in solution B in 1.0 M KOH solution. The overpotential (η_{10}) to the standard potential of $2H_2O = O_2 + 4H^+ + 4e$ (1.23 V vs. RHE), corresponding to the current density of 10 mA/cm^2, was used to evaluate OER activity. Compared to 628 mV on Cu, the overpotential of 325–332 mV in coating B shows high catalytic activity. Such overpotentials are apparently smaller than that of RuO_2 (343 mV). Furthermore, the Tafel slope (39.1–44.3 mV/decade) is also extremely lower than those of copper (125.4 mV/decade) and RuO_2 (66.0 mV/decade). These results indicate the potential for using oxygen-carbon-contained CrMnFeCoNi coating instead of expensive RuO_2. Plenty of oxygen or carbon vacancies might have been produced due to the different oxidation states of Cr, Mn, Fe, Co, and Ni in the coating, which attributed to this low overpotential for OER.

At the next stage of this study, the detailed structure of the above coatings will be further explored, and the mechanism of the OER reaction will be investigated. Moreover, the solution condition for deposition should be modified to control the composition of the coatings to achieve high purity of entropy alloys or higher activation and stability for the OER catalysis.
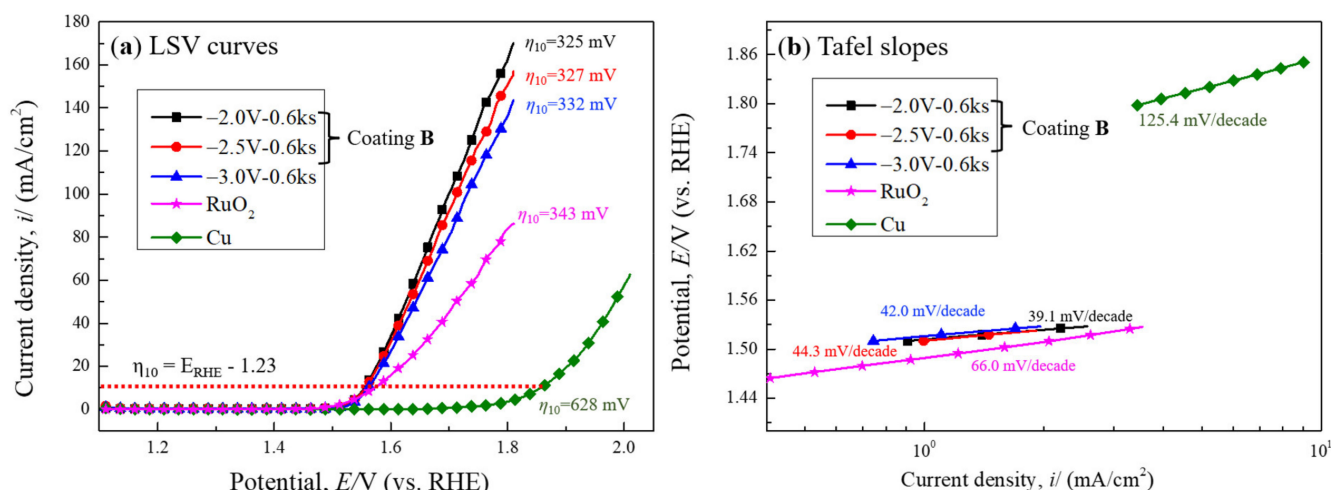
Figure 12. Polarization LSV curves (**a**) and Tafel slopes (**b**) of Cu, RuO_2, and coating B deposited at −2.0 V, −2.5 V, and −3.0 V (vs. SSE) for 0.6 ks.

4. Conclusions

Two oxygen-carbon-contained CrMnFeCoNi coatings were prepared by electrodeposition in an organic solvent of DMF-CH_3CN with chlorides of chromium, manganese, iron, cobalt, and nickel. Supporting electrolyte $LiClO_4$ was included or excluded from the bath solution to investigate the effect of lithium ion. The composition and structure of the coatings were investigated, and the deposition process was discussed. Finally, mechanical and electrocatalytic properties were investigated. The obtained results were as follows:

(1) In the presence of $LiClO_4$ in the bath solution, lithium was contained in the coating and existed as the oxidized state of Li_2CO_3 and Li_2O. This made the instability of the coating, which can be easily delaminated in water. Therefore, $LiClO_4$ was unsuitable as a supporting electrolyte in the current deposition.

(2) In the absence of $LiClO_4$ in the bath solution, stable coatings were obtained by enhancing concentrations of target metal ions and applying constant potentials at −2.0, −2.5, and −3.0 V (vs. SSE). Resultant coatings were confirmed to be amorphous and nanocrystalline, containing more than half of oxygen and carbon atoms and near-equal ratios of Cr, Mn, Fe, Co, and Ni.

(3) Full oxide/hydroxide of Cr and Mn, most oxide/hydroxide of Fe, half oxide/hydroxide of Co, and some oxide/hydroxide of Ni composed the coatings obtained in the bath without $LiClO_4$, giving entropies of metal elements near or larger than 1.5 R.

(4) The oxygen-carbon-contained coating CrMnFeCoNi obtained in the bath without $LiClO_4$ showed a high hardness level and advanced electrocatalytic activity in the oxygen evolution reaction.

(5) The electrodeposition process in DMF-CH_3CN with chlorides of chromium, manganese, iron, cobalt, and nickel is complex, concerning not only the reduction of cations but also the intervention of chemical reaction from the solvent.

Author Contributions: T.X. fabricated and characterized the coatings. R.W. designed and supervised the study. E.T. conducted the TEM and TOF-SIMS analysis. T.X. and R.W. discussed and wrote the paper. Y.S., M.B., Y.L. and Z.L. were involved in data interpretation. All authors have read and agreed to the published version of the manuscript.

Institutional Review Board Statement: Not applicable.

Informed Consent Statement: Not applicable.

Data Availability Statement: Not applicable.

Conflicts of Interest: The authors declare no competing interests.

References

1. Yeh, J.W.; Chen, S.K.; Lin, S.J.; Gan, J.Y.; Chin, T.S.; Shun, T.T.; Tsau, C.H.; Chang, S.Y. Nanostructured high-entropy alloys with multiple principal elements: Novel alloy design concepts and outcomes. *Adv. Eng. Mater.* **2004**, *6*, 299–303. [CrossRef]
2. Cantor, B.; Chang, I.T.H.; Knight, P.; Vincent, A.J.B. Microstructural development in equiatomic multicomponent alloys. *Mater. Sci. Eng. A* **2004**, *375–377*, 213–221. [CrossRef]
3. Zhang, Y.; Zuo, T.; Tang, Z.; Gao, C.M.; Dahmen, K.A.D.; Liaw, P.K.; Lu, Z. Microstructures and properties of high-entropy alloys. *Prog. Mater. Sci.* **2014**, *61*, 1–93. [CrossRef]
4. Feng, X.; Tang, G.; Sun, M.; Ma, X.; Wang, L.; Yukimura, K. Structure and properties of multi-targets magnetron sputtered ZrNbTaTiW multi-elements alloy thin films. *Surf. Coat. Technol.* **2013**, *228*, S424–S427. [CrossRef]
5. Zhang, S.; Han, B.; Li, M.; Hu, C.; Zhang, Q.; Liu, X.; Wang, Y. Investigation on microstructure and properties of laser cladded AlCoCrCuFeNi high entropy alloy coating by ultrasonic impact treatment. *Intermetallics* **2021**, *128*, 107017. [CrossRef]
6. Qiu, X.; Zhang, Y.; Liu, C. Effect of Ti content on structure and properties of Al2CrFeNiCoCuTix high-entropy alloy coatings. *J. Alloys Compd.* **2014**, *585*, 268–282. [CrossRef]
7. Sistla, H.R.; Newkirk, J.W.; Liou, F.F. Effect of Al/Ni ratio, heat treatment on phase transformations and microstructure of $Al_xFeCoCrNi_{2-x}$ (x = 0.3, 1) high entropy alloys. *Mater. Des.* **2015**, *81*, 113–121. [CrossRef]
8. Wang, C.; Yu, Y.; Zhang, H.; Xu, L.; Ma, X.; Wang, F.; Song, B. Microstructure and corrosion properties of laser remelted CrFeCoNi and CrMnFeCoNi high entropy alloys coatings. *J. Mater. Res. Tech.* **2021**, *15*, 5187–5196. [CrossRef]
9. Sugita, K.; Ogawa, R.; Mizuno, M.; Araki, H.; Yabuuchi, A. Vacancy migration energies in CrMnFeCoNi, CrFeCoNi, and CrFeNi alloys and their effect on atomic diffusion. *Scr. Mater.* **2022**, *208*, 114339. [CrossRef]
10. Zhang, M.; George, E.P.; Gibeling, J.C. Elevated-temperature deformation mechanisms in a CrMnFeCoNi high-entropy alloy. *Acta Mater.* **2021**, *218*, 117181. [CrossRef]
11. Daniel, R.; Zalesak, J.; Matko, I.; Baumegger, W.; Hohenwarter, A.; George, E.P.; Keckes, J. Microstructure-dependent phase stability and precipitation kinetics in equiatomic CrMnFeCoNi high-entropy alloy: Role of grain boundaries. *Acta Mater.* **2022**, *223*, 117470. [CrossRef]
12. Zhang, Y.; Lu, T.; Ye, Y.; Dai, W.; Zhu, Y.; Pan, Y. Stabilizing oxygen vacancy in entropy-engineered $CoFe_2O_4$-type catalysts for co-prosperity of efficiency and stability in an oxygen evolution reaction. ACS Appl. *Mater. Inter.* **2020**, *12*, 32548–32555. [CrossRef]
13. Li, Q.H.; Yue, T.M.; Guo, Z.N. Electro-spark deposition of multi-element high entropy alloy coating. *Mater. Sci. Tech.* **2022**, *3*, 1538–1547.
14. Yu, R.S.; Huang, C.J.; Huang, R.H.; Sun, C.H.; Shieu, F.S. Structure and optoelectronic properties of multi-element oxide thin film. *Appl. Surf. Sci.* **2011**, *257*, 6073–6078. [CrossRef]
15. Shen, W.J.; Tsai, M.H.; Chang, Y.S.; Yeh, J.W. Effects of substrate bias on the structure and mechanical properties of $(Al_{1.5}CrNb_{0.5}Si_{0.5}Ti)N_x$ coatings. *Thin Solid Films* **2012**, *520*, 6183–6188. [CrossRef]
16. Huang, P.K.; Yeh, J.W. Effects of substrate bias on structure and mechanical properties of (AlCrNbSiTiV)N coatings. *J. Phys. D Appl. Phys.* **2009**, *42*, 115401–115407. [CrossRef]
17. Chang, Z.C.; Liang, S.C.; Han, S.; Chen, Y.K.; Shieu, F.S. Characteristics of TiVCrAlZr multi-element nitride films prepared by reactive sputtering. *Nucl. Instrum. Methods Phys. Res. Sect. B Beam Interact. Mater. At.* **2010**, *268*, 2504–2509. [CrossRef]
18. Yao, C.Z.; Zhang, P.; Liu, M.; Li, G.; Ye, J.; Liu, P.; Tong, Y. Electrochemical preparation and magnetic study of Bi–Fe–Co–Ni–Mn high entropy alloy. *Electrochim. Acta* **2008**, *53*, 8359–8365. [CrossRef]
19. Yao, C.Z.; Zhang, P.; Tong, Y.; Xia, D.; Ma, H. Electrochemical synthesis and magnetic studies of Ni-Fe-Co-Mn-Bi-Tm high entropy alloy film. *Chem. Res. Chin. Univ.* **2010**, *26*, 640–644.
20. Yao, C.Z.; Ma, H.; Tong, Y. Electrochemical preparation and magnetic study of amorphous nanostructured Nd-Fe-Co-Ni-Mn high entropy alloy film. *Chin. J. Appl. Chem.* **2011**, *28*, 1189–1194.
21. Li, H.; Sun, H.; Wang, C.; Wei, B.; Yao, C.Z.; Tong, Y.; Ma, H. Controllable electrochemical synthesis and magnetic behaviors of Mg–Mn–Fe–Co–Ni–Gd alloy films. *J. Alloys Compd.* **2014**, *598*, 161–165. [CrossRef]
22. Zheng, M.; Li, Y.; Hu, J.; Zhao, Y.; Yu, L. Preparation of high entropy alloy thin film fenicobimn by electroplating deposition method. *Mater. Sci.* **2014**, *11*, 344–348.

23. Soare, V.; Buradaa, M.; Constantin, I.; Mitrică, D.; Bădiliță, V.; Caragea, A.; Târcolea, M. Electrochemical deposition and microstructural characterization of AlCrFeMnNi and AlCrCuFeMnNi high entropy alloy thin films. *Appl. Surf. Sci.* **2015**, *358*, 533–539. [CrossRef]

24. House, J.E., Jr.; Reif, L.A., Jr.; House, J.D. A relationship between hydration enthalpies and ionization energies of metal ions. *Thermochim. Acta* **1983**, *66*, 365–368. [CrossRef]

25. Tezuka, M. Electrolytic reduction of oxygen molecules. *Chem. Educ.* **1998**, *46*, 222–225.

26. Gürbüz, E.; Albin, V.; Lair, V.; Ringuedé, A.; Cassir, M. Oxidation behavior of H_2 and CO produced by H_2O and/or CO_2 reduction in molten carbonates: Effect of gas environment and hydroxides. *Electrochim. Acta* **2021**, *395*, 139202. [CrossRef]

27. Tang, Q.; Dai, X.; Wang, Z.; Wu, F.; Mai, Y.; Gu, Y.; Deng, Y. Enhanced high-voltage performance of $LiCoO_2$ cathode by directly coating of the electrode with Li_2CO_3 via a wet chemical method. *Ceram. Int.* **2021**, *47*, 19374–19383. [CrossRef]

28. Wang, R.G.; Li, Y.H.; Xiao, T.; Cong, L.; Ling, Y.H.; Lu, Z.X.; Fukushima, C.; Tsuchitori, I.; Bazzaoui, M. Using atomic force microscopy to measure thickness of passive film on stainless steel immersed in aqueous solution. *Sci. Rep.* **2019**, *9*, 13094. [CrossRef]

29. Protsenko, V.; Danilov, F. Kinetics and mechanism of chromium electrodeposition from formate and oxalate solutions of Cr (III) compounds. *Electrochim. Acta* **2009**, *54*, 5666–5672. [CrossRef]